Editors' Suggestion

Magnetoelectric Classification of Skyrmions

Sayantika Bhowal* and Nicola A. Spaldin
Materials Theory, ETH Zurich, Wolfgang-Pauli-Strasse 27, 8093 Zurich, Switzerland

(Received 17 January 2022; accepted 6 May 2022; published 3 June 2022)

We develop a general theory to classify magnetic skyrmions and related spin textures in terms of their magnetoelectric multipoles. Since magnetic skyrmions are now established in insulating materials, where the magnetoelectric multipoles govern the linear magnetoelectric response, our classification provides a recipe for manipulating the magnetic properties of skyrmions using applied electric fields. We apply our formalism to skyrmions and antiskyrmions of different helicities, as well as to magnetic bimerons, which are topologically, but not geometrically, equivalent to skyrmions. We show that the nonzero components of the magnetoelectric multipole and magnetoelectric response tensors are uniquely determined by the topology, helicity, and geometry of the spin texture. Therefore, we propose straightforward linear magnetoelectric response measurements as an alternative to Lorentz microscopy for characterizing insulating skyrmionic textures.

DOI: 10.1103/PhysRevLett.128.227204

The concept of skyrmions, originally invoked by Skyrme to describe the stability of hadrons in particle physics more than half a century ago [1,2], has found fertile ground in condensed matter systems as diverse as liquid crystals [3], Bose-Einstein condensates [4,5], quantum Hall systems [6], and helimagnets [7–11]. The magnetic skyrmions that form in the latter are metastable, topologically protected, nanometer-sized, swirling spin textures, with potential application as data bits in future high-density data storage devices [12–14].

Magnetic skyrmions have been found in bulk chiral and polar magnets [9,10,15–21], thin film heterostructures [13,14,22], and multilayer nanostructures, [23–29]. Their radially symmetric spin texture is described by a local magnetization vector $\hat{n}(\theta(r),\phi(\alpha))$, with $\theta(r)$ and $\phi(\alpha)$ characterizing the radial profile and the twisting angle, respectively, while the skyrmion number $N_{sk} = (1/4\pi)\int dxdy\hat{n}\cdot(\partial_x\hat{n}\times\partial_y\hat{n})$ characterizes the topology of the spin texture and manifests in the various exotic topological transport properties [30–32]. For example, the topological invariants $N_{sk} = \pm 1$ represent the skyrmion and the antiskyrmion, respectively [see Figs. 1(a) and 1(b)].

In addition to their well-explored topological order, the lack of both space-inversion $\mathcal{I}$ and time-reversal τ symmetries in skyrmionlike spin textures makes them potential hosts for magnetoelectric (ME) multipoles [33,34], formally defined as $\mathcal{M}_{ij} = \int r_i\mu_j(\vec{r})d^3r$, with $\vec{\mu}(\vec{r})$ being the magnetization density. The three irreducible (IR) components of the $\mathcal{M}_{ij}$ tensor, the ME monopole (a), toroidal moment ($\vec{t}$), and the ME quadrupole moment q_{ij}, are quintessential to the linear ME response α_{ij}, which is the generation of magnetization (polarization) by an applied electric (magnetic) field. They have also been associated with other exciting properties and phases of matter, including hidden "ferrotoroidic" order [35–37], current induced Néel vector switching in antiferromagnetic spintronics [38,39], and even with axionic dark matter [40]. The recent observation [15–21] of skyrmions in insulators opens the door to combined electric and magnetic field manipulation of the skyrmions, mediated via these ME multipoles (MEMs).

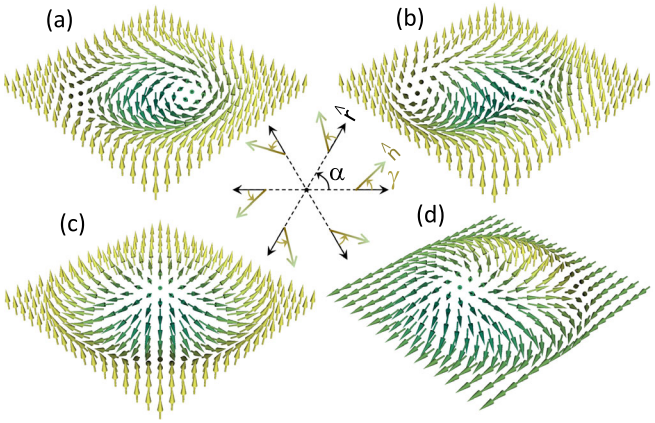

FIG. 1. (a) Bloch skyrmion and (b) antiskyrmion, (c) Néel skyrmion, and (d) bimeron. The schematic at the center illustrates the helicity γ, with gradient-colored arrows indicating the in-plane components of $\hat{n}$.

Published by the American Physical Society under the terms of the Creative Commons Attribution 4.0 International license. Further distribution of this work must maintain attribution to the author(s) and the published article's title, journal citation, and DOI.

TABLE I. ME classification of skyrmions, antiskyrmions, and bimerons. Only independent multipolization components are listed.

	Skyrmions		Antiskyrmions		Bimerons	
Properties	$\gamma = 0$ (Néel)	$\gamma = \pi/2$ (Bloch)	$\gamma = 0$	$\gamma = \pi/2$	$\gamma = 0$	$\gamma = \pi/2$
ME multipolization	$\mathcal{A} \propto \cos\gamma$	$\mathcal{T}_z \propto \sin\gamma$	$\mathcal{Q}_{x^2-y^2} \propto \cos\gamma$	$\mathcal{Q}_{xy} \propto \sin\gamma$	$\mathcal{Q}_{x^2-y^2} \propto \cos\gamma$	$\mathcal{T}_x \propto \sin\gamma$
ME polarizability	$\alpha_{xx} = \alpha_{yy}$	$\alpha_{xy} = -\alpha_{yx}$	$\alpha_{xx} = -\alpha_{yy}$	$\alpha_{xy} = \alpha_{yx}$	$\alpha_{xz} = -\alpha_{yy}$	$\alpha_{xy} = \alpha_{yz}$

In spite of this intriguing connection, to our knowledge, the only link between MEMs and skyrmions mentioned to date is to their toroidization $\mathcal{T}_z$ (toroidal moment per unit volume, $\vec{t}/V$) [41]. Here we present a complete ME classification of skyrmions and antiskyrmions with different helicities γ (see Fig. 1), as well as magnetic bimerons [see Fig. 1(d)] taking all components of the magnetoelectric multipolization (that is the MEM per unit volume) into account. We find that the ME monopolization $\mathcal{A}$ (ME monopole per unit volume, a/V) and the quadrupolization $\mathcal{Q}_{ij}$ (quadrupole moment per unit volume, q_{ij}/V) can be nonzero, in addition to the toroidization $\vec{\mathcal{T}}$, with the form of the MEM tensor depending on both the topology and geometry of the spin texture. These distinct MEMs in skyrmions, antiskyrmions, and bimerons, further, manifest in the corresponding ME polarizability α_{ij}, implying that the skyrmion type can be determined from a straightforward magnetoelectric measurement and pointing to combined electric- and magnetic-field control of skyrmions.

The main outcomes of the classification are given in Table I, which summarizes the key findings of our work. First, while skyrmions with different helicities carry the same topological order (N_{sk}) and are, therefore, topologically indistinguishable, they have different MEMs, which, in turn, leads to different ME polarizability α_{ij}. As a result, the ME polarizability can be used as an alternative to Lorentz microscopy [10] to classify skyrmions with different helicities. Second, skyrmions and antiskyrmions differ not only in their topological order, but also have different MEMs and, hence, different ME response. Therefore, skyrmions and antiskyrmions can be characterized and detected in experiments using a single observable α_{ij}. The case of the bimeron emphasizes the strong dependence of the form of the MEM and α_{ij} tensors on the geometry of the spin texture. Finally, the unique spin textures of skyrmions and antiskyrmions facilitate the existence of multipolization components in their purest form. For example, Bloch skyrmions have a pure toroidization $\mathcal{T}_z$, antiskyrmions with $\gamma = \pi/2$ have a pure quadrupolization $\mathcal{Q}_{xy}$, etc. Such a pure toroidal or quadrupolar state is rather rare in materials with magnetic order on the unit-cell scale, where they often coexist with each other due to symmetry [34,35,42–44].

ME multipolization and spin geometry in two dimensions.—Here we briefly review the ME multipolization and discuss the dependence of the multipolization tensor on the lattice dimension and the spin geometry of the usual two-dimensional (2D) topological skyrmionlike spin texture.

The ME multipolization $\tilde{\mathcal{M}}_{ij} = \mathcal{M}_{ij}/V$, i.e., the MEM moment per unit volume V, describes the first-order asymmetry in the magnetization density $\vec{\mu}(\vec{r})$ that couples to derivatives of the magnetic field [34,45]. Hereafter, we only consider the spin magnetic moment. As stated earlier, the $\mathcal{M}_{ij}$ tensor has three IR components [34]: (a) the scalar ME monopole $a = \frac{1}{3}\mathcal{M}_{ii} = \int \vec{r}\cdot\vec{\mu}(\vec{r})d^3r$, (b) the ME toroidal moment $t_i = \frac{1}{2}\varepsilon_{ijk}\mathcal{M}_{jk} = \frac{1}{2}\int \vec{r}\times\vec{\mu}(\vec{r})d^3r$, and (c) the symmetric traceless five component quadrupole moment tensor $q_{ij} = \frac{1}{2}(\mathcal{M}_{ij} + \mathcal{M}_{ji} - \frac{2}{3}\delta_{ij}\mathcal{M}_{kk}) = \frac{1}{2}\int(r_i\mu_j + r_j\mu_i - \frac{2}{3}\delta_{ij}\vec{r}\cdot\vec{\mu})d^3r$. The ME monopole and the $q_{x^2-y^2}$ and q_{z^2} quadrupole moment components form the diagonal of the $\mathcal{M}_{ij}$ tensor, while the symmetric and the antisymmetric parts of the off-diagonal elements are represented by the q_{xy}, q_{xz}, and q_{yz} quadrupole moments and $\vec{t}$, respectively.

We now point out some interesting features of the $\mathcal{M}_{ij}$ tensor based on the reduced lattice dimension from 3D to 2D and the spin geometry. First, a 2D in-plane lattice directly implies vanishing $\mathcal{M}_{zi} = \int z\mu_i d^2r$ components and the corresponding multipolization (which in this case is multipole moment per unit area S, $\tilde{\mathcal{M}}_{ij} = \mathcal{M}_{ij}/S$). Here $i = x$, y, and z are the Cartesian components of $\vec{\mu}$. Moreover, the radially symmetric μ_z spin component at each lattice site of a skyrmion crystal forces the $\mathcal{M}_{iz} = \int r_i\mu_z d^2r$ components to vanish. The resulting $\mathcal{M}_{ij}$ tensor can therefore be written as a 2×2 matrix of nonzero components [see Fig. 2(a)]. In contrast, the absence of μ_z radial symmetry in a bimeron texture means that the $\mathcal{M}_{ij}$ tensor does not reduce to a 2×2 matrix. The different dimensionality of their $\mathcal{M}_{ij}$ tensors emphasizes that, although topologically equivalent, skyrmions and bimerons have distinct ME responses originating from geometrical differences. Second, in a 2D lattice, the ME monopole a and the quadrupole q_{z^2} are equal and opposite to each other: $a = \frac{1}{3}\int d^2r(x\mu_x + y\mu_y + z\mu_z) = \frac{1}{3}\int d^2r(x\mu_x + y\mu_y)$, and $q_{z^2} = \frac{1}{2}\int d^2r\{z\mu_z + z\mu_z - \frac{2}{3}(x\mu_x + y\mu_y)\} = -\frac{1}{3}\int d^2r(x\mu_x + y\mu_y) = -a$. This means that in a 2D lattice q_{z^2} ($\mathcal{Q}_{z^2}$) is the same as an anti-a (anti-$\mathcal{A}$) and vice versa [see Figs. 2(b) and 2(c)].

Results and discussion.—We begin by considering a tight-binding model for an electron in a square lattice of spin texture $\hat{n}_i$ [46],

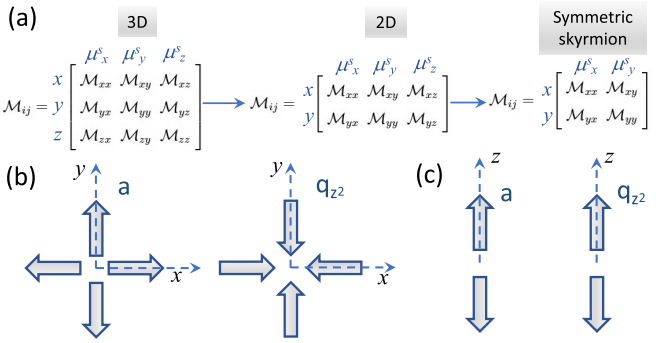

FIG. 2. (a) Schematics showing the evolution of the $\mathcal{M}_{ij}$ tensor as the structural dimension reduces from 3D to 2D, and finally for the specific radially symmetric skyrmion spin texture. Representative spin magnetic moment arrangements (shown in arrows) for a ME monopole a and the quadrupole moment q_{z^2} in the (b) $x-y$ plane and (c) along z, showing that a and q_{z^2} in (b) are exactly equal and opposite in the absence of a local z coordinate.

$$\mathcal{H} = t\sum_{\langle i,j\rangle} c_i^\dagger c_j - J_H \sum_i \hat{n}_i \cdot (c_i^\dagger \vec{\sigma} c_i). \tag{1}$$

Here, t and J_H are the nearest-neighbor hopping and Hund's coupling, respectively. For a skyrmion texture, $\hat{n}_i \equiv (\sin\theta_i(r_i)\cos\phi_i(\alpha_i), \sin\theta_i(r_i)\sin\phi_i(\alpha_i), \cos\theta_i(r_i))$ with $\theta_i = \pi(1 - r_i/\lambda)$ [31] and $\phi_i = m\alpha_i + \gamma$. Here, the vorticity $m = \pm 1$ corresponds to a skyrmionic and an antiskyrmionic state, respectively, while the helicity γ can take different values; e.g., $\gamma = 0$ and $\pi/2$ correspond to Bloch and Néel skyrmions, respectively [see Figs 1(a) and 1(c)]. The bimeron configuration [see Fig. 1(d)] can be generated by $(\pi/2)$ rotation of the skyrmion spins around an in-plane axis [47]. Although the explicit results may depend on the choice of the in-plane rotation axis, here to demonstrate the crucial spin geometry dependence, we consider the y-axis rotation $(\hat{n}_x, \hat{n}_y, \hat{n}_z) \to (\hat{n}_z, \hat{n}_y, -\hat{n}_x)$, losing thereby the radial symmetry of the spin-z component of a skyrmion while keeping the topology intact [48,49].

In the adiabatic limit ($J_H \gg t$), the low-lying bands of the tight-binding model (1) can be approximated as [46]

$$\mathcal{H} = \sum_{\langle i,j\rangle} t_{ij}^{\text{eff}} d_i^\dagger d_j, \tag{2}$$

where $d_i, d_i^\dagger$ are spinless operators, and $t_{ij}^{\text{eff}} = t\cos(\tilde{\theta}_{ij}/2)e^{ia_{ij}}$ is an effective hopping that depends on the twisting angle difference $(\phi_i - \phi_j)$ (see Supplemental Material [50]).

We first analyze the band structures of 2D periodic crystals of skyrmions, bimerons, and antiskyrmions, computed from the tight-binding model (1). The low-lying bands for $J_H/t = 10$, shown in Fig. 3(a), are well described by the adiabatic limit Hamiltonian of Eq. (2) and are identical for the three topological spin textures for a given set of parameters. This is because the effective hopping t_{ij}^{eff}

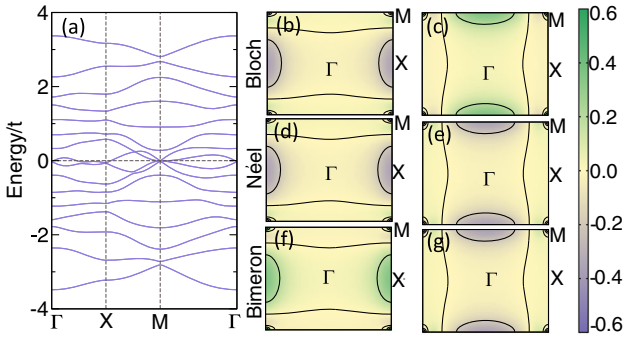

FIG. 3. (a) Band structure for the model Hamiltonian (1) with parameter $J_H/t = 10$. For simplicity, the lowest 16 bands of the model Hamiltonian (1) around the energy $E = -J_H/t$ are shown and the energies are shifted by E, indicated by the horizontal dashed line. (b)–(g) Momentum space distribution of $\mathcal{O}_{ij}(\vec{k})$ of Eq. (3). (b) $\mathcal{O}_{xy}(\vec{k})$ and (c) $\mathcal{O}_{yx}(\vec{k})$ for the Bloch skyrmion; (d) $\mathcal{O}_{xx}(\vec{k})$ and (e) $\mathcal{O}_{yy}(\vec{k})$ for the Néel skyrmion; (f) $\mathcal{O}_{xz}(\vec{k})$ and (g) $\mathcal{O}_{yy}(\vec{k})$ for the bimeron. The Fermi energy is taken to be at the top of the lowest band in (a).

depends only on the difference in ϕ and, therefore, remains the same for any constant rotation of the spins. Since Néel and Bloch skyrmions differ only in helicity γ, and bimerons by a $(\pi/2)$ rotation around the y axis, they therefore have the same t_{ij}^{eff}. For antiskyrmions, t_{ij}^{eff} has the opposite phase, leading to opposite topological order while keeping the band energies unaltered.

While the band structure is insensitive to rotations of the spins, they manifest in the corresponding spin multipolization $\tilde{\mathcal{M}}_{ij}$, which can be computed as the Brillouin zone (BZ) integration over all the occupied states n of $\mathcal{O}_{ij}^n(\vec{k})$ [45,53],

$$\tilde{\mathcal{M}}_{ij} = -g\mu_B \int^{occ} \frac{d^2k}{(2\pi)^2} \sum_n \mathcal{O}_{ij}^n(\vec{k}), \qquad \text{where}$$

$$\mathcal{O}_{ij}^n(\vec{k}) = \sum_{m\neq n} (\varepsilon_n + \varepsilon_m - 2\varepsilon_F)\,\text{Im}\left[\frac{\langle n|v_i|m\rangle\langle m|s_j|n\rangle}{(\varepsilon_n - \varepsilon_m)^2}\right]. \tag{3}$$

Here v_i and s_i are the velocity and the Pauli spin operators, respectively.

We compute the $\tilde{\mathcal{M}}_{ij}$ tensor for γ values ranging from $-\pi$ to π, assuming that only the lowest band in Fig. 3(a) is occupied. We start with the case of the skyrmion crystal and discuss pure Bloch- and Néel-type skyrmions first, before analyzing intermediate γ values. Our calculations show that the Bloch skyrmions have only nonzero off-diagonal elements, $\tilde{\mathcal{M}}_{xy} = -\tilde{\mathcal{M}}_{yx}$, indicating the presence of only the toroidization $\mathcal{T}_z$, consistent with Ref. [41]. We note that a pure $\mathcal{T}_z$ is unusual [34,35,42–44]; while recently we demonstrated a pure toroidal moment in the reciprocal space of $PbTiO_3$ [54], to the best of our knowledge this is the first prediction of a pure toroidal moment in a real-space

spin texture. In complete contrast, Néel skyrmions have only nonzero diagonal elements, $\tilde{\mathcal{M}}_{xx} = \tilde{\mathcal{M}}_{yy}$. Since the ME monopolization $\mathcal{A}$ and quadrupolization $\mathcal{Q}_{x^2-y^2}$ and $\mathcal{Q}_{z^2}$ contribute to the diagonal elements as

$$\begin{aligned}\tilde{\mathcal{M}}_{xx} &= \mathcal{A} + \frac{1}{2}(\mathcal{Q}_{x^2-y^2} - \mathcal{Q}_{z^2}),\\ \tilde{\mathcal{M}}_{yy} &= \mathcal{A} - \frac{1}{2}\mathcal{Q}_{x^2-y^2} - \frac{1}{2}\mathcal{Q}_{z^2},\\ \tilde{\mathcal{M}}_{zz} &= \mathcal{A} + \mathcal{Q}_{z^2}, \end{aligned} \tag{4}$$

this implies the presence of a ME monopolization $\mathcal{A} = -\mathcal{Q}_{z^2}$ in a Néel skyrmion, consistent with our previous discussion that $a = -q_{z^2}$ in a 2D system.

In Figs. 3(b)–3(e), we show the k-space distributions of $\mathcal{O}_{ij}(\vec{k})$ for Bloch and Néel skyrmions. It is interesting to point out the multipolization symmetries, $\mathcal{O}_{xy}^{\text{Bloch}}(\vec{k}) = \mathcal{O}_{xx}^{\text{Néel}(\vec{k})}$, $\mathcal{O}_{yx}^{\text{Bloch}}(\vec{k}) = -\mathcal{O}_{yy}^{\text{Néel}(\vec{k})}$, which follow from the differences in γ: $\mu_y^{\text{Bloch}} = \sin\theta\sin(\pi/2+\phi) = \mu_x^{\text{Néel}}$. Furthermore, since the velocity v_x does not depend on γ, it is easy to see from Eq. (3) that $\mathcal{O}_{xy}^{\text{Bloch}} = \mathcal{O}_{xx}^{\text{Néel}}$. Similarly, it can be shown that $\mu_x^{\text{Bloch}} = -\mu_y^{\text{Néel}}$, leading to $\mathcal{O}_{yx}^{\text{Bloch}}(\vec{k}) = -\mathcal{O}_{yy}^{\text{Néel}(\vec{k})}$.

It is important to point out that, although the explicit value of $\mathcal{O}_{ij}$ depends on the choice of lattice geometry, Fermi energy ε_F [see Eq. (3)], and the Hamiltonian parameters, the relations discussed here are independent of these properties because they are solely determined by the symmetries of the skyrmion spin texture. Thus, our results, governed by symmetries, are general and hold for other skyrmion lattices with different geometries, such as triangular and hexagonal lattices, as well.

Finally, for twisted skyrmions described by intermediate γ values, we find that both diagonal and off-diagonal elements of $\tilde{\mathcal{M}}_{ij}$ exist, resulting in nonzero $\mathcal{T}_z$ and $\mathcal{A} = -\mathcal{Q}_{z^2}$, that vary periodically with γ [see Fig. 4(a)]. While $\mathcal{T}_z$ varies as $\sin\gamma$, $\mathcal{A}$ ($\mathcal{Q}_{z^2}$) varies as $\cos\gamma$. These periodic dependences of $\mathcal{T}_z$ and $\mathcal{A}$ ($\mathcal{Q}_{z^2}$) can be understood from their formal definitions. For example, $\mathcal{T}_z = t_z/S$, with $t_z = \int d^2r(\vec{r}\times\vec{\mu})$. For skyrmions $\vec{\mu} \equiv (\sin\theta\cos\phi, \sin\theta\sin\phi, \cos\theta)$, with $\phi(\alpha) = \alpha + \gamma$, and $(x, y) \equiv r(\cos\alpha, \sin\alpha)$. Substituting this expression for $\vec{\mu}$, we obtain $\mathcal{T}_z \propto \sin\gamma$. Similarly, the ME monopolization $\mathcal{A} = a/S = (1/S)\int d^2r(\vec{r}\cdot\vec{\mu}) \propto \cos\gamma$.

The spin multipolization, discussed above, is directly related to the spin ME polarizability, $\alpha_{ij} = -e(\partial\tilde{\mathcal{M}}_{ij}/\partial\varepsilon_F)$, which can, therefore, be computed as [45]

$$\begin{aligned}\alpha_{ij} &= eg\mu_B \int^{occ} \frac{d^2k}{(2\pi)^2}\sum_n \mathcal{D}_{ij}^n(\vec{k}),\\ \text{where } \mathcal{D}_{ij}^n(\vec{k}) &= -2\text{Im}\sum_{m\neq n}\left[\frac{\langle n|v_i|m\rangle\langle m|s_j|n\rangle}{(\varepsilon_n - \varepsilon_m)^2}\right]. \end{aligned} \tag{5}$$

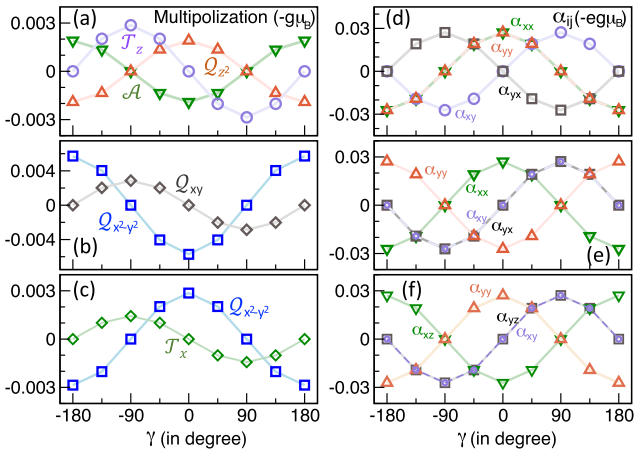

FIG. 4. Variation in the ME multipolization components as a function of the helicity γ in (a) skyrmions, (b) antiskyrmions, and (c) bimerons. The same variation for the ME polarizability components α_{ij} in (d) skyrmions, (e) antiskyrmions, and (f) bimerons.

Here the integration is over the occupied part of the BZ. We compute the response α_{ij} for the skyrmion as a function of γ and show our results in Fig. 4(d). Similar to the $\tilde{\mathcal{M}}_{ij}$ tensor, we find that α_{ij} has a 2×2 matrix form, with $\alpha_{xx} = \alpha_{yy}$ varying as $\cos\gamma$ and $\alpha_{xy} = -\alpha_{yx}$ as $\sin\gamma$ [see Fig. 4(d)], reflecting the one-to-one correspondence between $\tilde{\mathcal{M}}_{ij}$ and α_{ij}. A similar sine-cosine dependence of α_{ij} was predicted earlier for magnetic vortices [55].

We now turn to the case of an antiskyrmion with vorticity $m = -1$. The variations of $\tilde{\mathcal{M}}_{ij}$ and α_{ij} with γ in an antiskyrmion are shown in Figs. 4(b) and 4(e). Similar to the case of skyrmions, at $\gamma = 0$, the $\tilde{\mathcal{M}}_{ij}$ tensor of an antiskyrmion has a diagonal 2×2 matrix form, but the diagonal elements have opposite signs, $\tilde{\mathcal{M}}_{xx} = -\tilde{\mathcal{M}}_{yy}$. Following Eq. (4), this implies the presence of quadrupolization $\mathcal{Q}_{x^2-y^2}$, which, as seen from Fig. 4(b), varies as $\cos\gamma$, with its maximum at $\gamma = 0$ and zero at $\gamma = \pi/2$. At $\gamma = \pi/2$, the $\tilde{\mathcal{M}}_{ij}$ tensor is off diagonal with $\tilde{\mathcal{M}}_{xy} = \tilde{\mathcal{M}}_{yx}$, in contrast to the opposite signs in skyrmions, leading to a quadrupolization $\mathcal{Q}_{xy}$ that varies as $\sin\gamma$. These periodic dependences again follow from the formal definitions: $\mathcal{Q}_{x^2-y^2} = (1/S)\int d^2r(x\mu_x - y\mu_y) \propto \cos\gamma$, noting that $\phi = -\alpha + \gamma$ for an antiskyrmion, and $\mathcal{Q}_{xy} = (1/2S)\int d^2r(x\mu_y + y\mu_x) \propto \sin\gamma$. The corresponding computed polarizability α_{ij} [Fig. 4(e)] follows the $\tilde{\mathcal{M}}_{ij}$ tensor, with $\alpha_{xx} = -\alpha_{yy} \propto \cos\gamma$ and $\alpha_{xy} = \alpha_{yx} \propto \sin\gamma$.

Finally, we discuss the bimeron crystal, motivated by its closely related spin texture to that of skyrmions. Despite being topologically equivalent to skyrmions, the lack of radial symmetry in the μ_z components of a bimeron texture results in a very different form of the $\tilde{\mathcal{M}}_{ij}$ tensor, emphasizing the crucial dependence on spin geometry. In contrast to the

skyrmions and antiskyrmions described above, the bimeron $\tilde{\mathcal{M}}_{ij}$ tensor has a 2×3 matrix form that corresponds to the middle panel of Fig. 2(a), with nonzero elements $\tilde{\mathcal{M}}_{xz} = -\tilde{\mathcal{M}}_{yy}$ at $\gamma = 0$. The nonzero elements of the $\tilde{\mathcal{M}}_{ij}$ tensor can be understood by noting that $\mu_z^{\text{bimeron}} = -\mu_x^{\text{Néel}}$, while $\mu_y^{\text{bimeron}} = \mu_y^{\text{Néel}}$. Since the velocities v_x and v_y are the same for both textures [they have identical band structures, Fig. 3(a)], this implies $\tilde{\mathcal{M}}_{xz}^{\text{bimeron}} = -\tilde{\mathcal{M}}_{xx}^{\text{Néel}}$ and $\tilde{\mathcal{M}}_{yy}^{\text{bimeron}} = \tilde{\mathcal{M}}_{yy}^{\text{Néel}}$, which is also reflected in the corresponding k-space distributions of $\mathcal{O}_{ij}(\vec{k})$, shown in Figs. 3(f) and 3(g), respectively. Consequently, $\tilde{\mathcal{M}}_{xx} = \tilde{\mathcal{M}}_{yy}$ in a Néel skyrmion translates into $\tilde{\mathcal{M}}_{xz} = -\tilde{\mathcal{M}}_{yy}$ in a bimeron. This further implies the presence of $\mathcal{Q}_{x^2-y^2} = 3\mathcal{Q}_{z^2} = -3\mathcal{A} = -2\mathcal{T}_y = 2\mathcal{Q}_{xz}$ at $\gamma = 0$. All the MEMs vary as $\cos\gamma$ with zero value at $\gamma = \pi/2$, at which nonzero elements are $\tilde{\mathcal{M}}_{xy} = \tilde{\mathcal{M}}_{yz}$, indicating the presence of $\mathcal{T}_x = \mathcal{Q}_{yz} = \mathcal{T}_z = \mathcal{Q}_{xy} \propto \sin\gamma$. The variation of the independent multipolization components with γ is shown in Fig. 4(c). A similar periodic dependence is also evident in the corresponding polarizability α_{ij}, shown in Fig. 4(f).

To summarize, we have introduced a ME classification of skyrmions and applied it to Bloch and Néel skyrmions [56], as well as antiskyrmions and bimerons. The formalism is general and can be extended to other spin textures. Our work opens the door for future works examining the implications of MEMs in both metallic and insulating skyrmionlike textures. In particular, dependence of the multipolization on the helicity demonstrated here may have useful implications in the context of recent efforts to control the helicity of skyrmions [57,58].

Note that the ME monopole associated with a Néel skyrmion in the present Letter is different from the previously predicted magnetic monopole at the point of coalescence of two ingoing skyrmion lines [59]. In particular, unlike the ME monopole, the magnetic monopole does not break inversion symmetry and appears in the zeroth-order term of the multipole expansion of a magnetization density in a magnetic field. However, care should be taken, as often in the literature this distinction based on formal definition is not followed. For example, as pointed out by Khomskii [60,61], the elementary excitation in spin ice that is referred to as a magnetic monopole carries an electric dipole (and so breaks space-inversion symmetry) in addition to a magnetic charge.

The proposed ME response of a skyrmion crystal may be probed using conventional ME measurement techniques [62,63]. Isolation of the response of the skyrmion crystal from the host may be challenging, but should be achievable by considering nonmultiferroic host materials. We hope that our work stimulates experimental efforts in ME manipulation of skyrmions and related topological spin textures, opening up new avenues in designing unique "skyrmionic" (skyrmion-based spintronic) devices with high-energy efficiency.

We thank Börge Göbel and Ingrid Mertig for insightful discussions. N. A. S. and S. B. were supported by the ERC under the EU's Horizon 2020 Research and Innovation Programme Grant No. 810451 and by ETH Zurich. Computational resources were provided by ETH Zurich's Euler cluster, and the Swiss National Supercomputing Centre, project ID eth3.

*Corresponding author.
sayantika.bhowal@mat.ethz.ch

[1] T. H. R. Skyrme and B. F. J. Schonland, Proc. R. Soc. A **260**, 127 (1961).
[2] T. Skyrme, Nucl. Phys. **31**, 556 (1962).
[3] D. C. Wright and N. D. Mermin, Rev. Mod. Phys. **61**, 385 (1989).
[4] T.-L. Ho, Phys. Rev. Lett. **81**, 742 (1998).
[5] T. Ohmi and K. Machida, J. Phys. Soc. Jpn. **67**, 1822 (1998).
[6] S. L. Sondhi, A. Karlhede, S. A. Kivelson, and E. H. Rezayi, Phys. Rev. B **47**, 16419 (1993).
[7] A. N. Bogdanov and D. A. Yablonski, Sov. Phys. JETP **68**, 101 (1989), http://www.jetp.ras.ru/cgi-bin/dn/e_068_01_0101.pdf.
[8] U. K. Rößler, A. N. Bogdanov, and C. Pfleiderer, Nature (London) **442**, 797 (2006).
[9] S. Mühlbauer, B. Binz, F. Jonietz, C. Pfleiderer, A. Rosch, A. Neubauer, R. Georgii, and P. Böni, Science **323**, 915 (2009).
[10] X. Z. Yu, Y. Onose, N. Kanazawa, J. H. Park, J. H. Han, Y. Matsui, N. Nagaosa, and Y. Tokura, Nature (London) **465**, 901 (2010).
[11] X. Z. Yu, N. Kanazawa, Y. Onose, K. Kimoto, W. Z. Zhang, S. Ishiwata, Y. Matsui, and Y. Tokura, Nat. Mater. **10**, 106 (2011).
[12] A. Fert, V. Cros, and J. Sampaio, Nat. Nanotechnol. **8**, 152 (2013).
[13] N. Romming, C. Hanneken, M. Menzel, J. E. Bickel, B. Wolter, K. von Bergmann, A. Kubetzka, and R. Wiesendanger, Science **341**, 636 (2013).
[14] S. Woo, K. Litzius, B. Krüger, M.-Y. Im, L. Caretta, K. Richter, M. Mann, A. Krone, R. M. Reeve, M. Weigand, P. Agrawal, I. Lemesh, M.-A. Mawass, P. Fischer, M. Kläui, and G. S. D. Beach, Nat. Mater. **15**, 501 (2016).
[15] S. Seki, X. Z. Yu, S. Ishiwata, and Y. Tokura, Science **336**, 198 (2012).
[16] T. Adams, A. Chacon, M. Wagner, A. Bauer, G. Brandl, B. Pedersen, H. Berger, P. Lemmens, and C. Pfleiderer, Phys. Rev. Lett. **108**, 237204 (2012).
[17] S. Seki, J.-H. Kim, D. S. Inosov, R. Georgii, B. Keimer, S. Ishiwata, and Y. Tokura, Phys. Rev. B **85**, 220406(R) (2012).
[18] I. Kézsmárki, S. Bordács, P. Milde, E. Neuber, L. M. Eng, J. S. White, H. M. Rønnow, C. D. Dewhurst, M. Mochizuki, K. Yanai, H. Nakamura, D. Ehlers, V. Tsurkan, and A. Loidl, Nat. Mater. **14**, 1116 (2015).
[19] Y. Fujima, N. Abe, Y. Tokunaga, and T. Arima, Phys. Rev. B **95**, 180410(R) (2017).

[20] S. Bordács, A. Butykai, B. G. Szigeti, J. S. White, R. Cubitt, A. O. Leonov, S. Widmann, D. Ehlers, H. A. K. von Nidda, V. Tsurkan, A. Loidl, and I. Kézsmárki, Sci. Rep. **7**, 7584 (2017).

[21] T. Kurumaji, T. Nakajima, V. Ukleev, A. Feoktystov, T.-h. Arima, K. Kakurai, and Y. Tokura, Phys. Rev. Lett. **119**, 237201 (2017).

[22] S. Heinze, K. von Bergmann, M. Menzel, J. Brede, A. Kubetzka, R. Wiesendanger, G. Bihlmayer, and S. Blügel, Nat. Phys. **7**, 713 (2011).

[23] C. Moreau-Luchaire, C. Moutafis, N. Reyren, J. Sampaio, C. A. F. Vaz, N. Van Horne, K. Bouzehouane, K. Garcia, C. Deranlot, P. Warnicke, P. Wohlhüter, J. M. George, M. Weigand, J. Raabe, V. Cros, and A. Fert, Nat. Nanotechnol. **11**, 444 (2016).

[24] R. Wiesendanger, Nat. Rev. Mater. **1**, 16044 (2016).

[25] A. O. Leonov, Y. Togawa, T. L. Monchesky, A. N. Bogdanov, J. Kishine, Y. Kousaka, M. Miyagawa, T. Koyama, J. Akimitsu, T. Koyama, K. Harada, S. Mori, D. McGrouther, R. Lamb, M. Krajnak, S. McVitie, R. L. Stamps, and K. Inoue, Phys. Rev. Lett. **117**, 087202 (2016).

[26] O. Boulle, J. Vogel, H. Yang, S. Pizzini, D. de Souza Chaves, A. Locatelli, T. O. Menteş, A. Sala, L. D. Buda-Prejbeanu, O. Klein, M. Belmeguenai, Y. Roussigné, A. Stashkevich, S. M. Chérif, L. Aballe, M. Foerster, M. Chshiev, S. Auffret, I. M. Miron, and G. Gaudin, Nat. Nanotechnol. **11**, 449 (2016).

[27] A. Soumyanarayanan, M. Raju, A. L. Gonzalez Oyarce, A. K. C. Tan, M.-Y. Im, A. P. Petrović, P. Ho, K. H. Khoo, M. Tran, C. K. Gan, F. Ernult, and C. Panagopoulos, Nat. Mater. **16**, 898 (2017).

[28] S. L. Zhang, G. van der Laan, W. W. Wang, A. A. Haghighirad, and T. Hesjedal, Phys. Rev. Lett. **120**, 227202 (2018).

[29] J. A. Garlow, S. D. Pollard, M. Beleggia, T. Dutta, H. Yang, and Y. Zhu, Phys. Rev. Lett. **122**, 237201 (2019).

[30] A. Neubauer, C. Pfleiderer, B. Binz, A. Rosch, R. Ritz, P. G. Niklowitz, and P. Böni, Phys. Rev. Lett. **102**, 186602 (2009).

[31] N. Nagaosa and Y. Tokura, Nat. Nanotechnol. **8**, 899 (2013).

[32] J. Matsuno, N. Ogawa, K. Yasuda, F. Kagawa, W. Koshibae, N. Nagaosa, Y. Tokura, and M. Kawasaki, Sci. Adv. **2**, e1600304 (2016).

[33] C. Ederer and N. A. Spaldin, Phys. Rev. B **76**, 214404 (2007).

[34] N. A. Spaldin, M. Fechner, E. Bousquet, A. Balatsky, and L. Nordström, Phys. Rev. B **88**, 094429 (2013).

[35] N. A. Spaldin, M. Fiebig, and M. Mostovoy, J. Phys. Condens. Matter **20**, 434203 (2008).

[36] H. Schmid, *Introduction to Complex Mediums for Optics and Electromagnetics*, edited by W. S. Weiglhoger and A. Lakhtakia (SPIE Press, Bellingham, WA, 2003), pp. 167–195.

[37] B. B. Van Aken, J.-P. Rivera, H. Schmid, and M. Fiebig, Nature (London) **449**, 702 (2007).

[38] H. Watanabe and Y. Yanase, Phys. Rev. B **98**, 245129 (2018).

[39] F. Thöle, A. Keliri, and N. A. Spaldin, J. Appl. Phys. **127**, 213905 (2020).

[40] H. S. Røising, B. Fraser, S. M. Griffin, S. Bandyopadhyay, A. Mahabir, S.-W. Cheong, and A. V. Balatsky, Phys. Rev. Research **3**, 033236 (2021).

[41] B. Göbel, A. Mook, J. Henk, and I. Mertig, Phys. Rev. B **99**, 060406(R) (2019).

[42] N. A. Spaldin, J. Exp. Theor. Phys. **159**, 594 (2021).

[43] S. Bhowal and N. A. Spaldin, Phys. Rev. Research **3**, 033185 (2021).

[44] S. Bhowal, D. O'Neill, M. Fechner, N. Spaldin, U. Staub, J. Duffy, and S. Collins, Open Res. Eur. **1**, 132 (2021).

[45] Y. Gao, D. Vanderbilt, and D. Xiao, Phys. Rev. B **97**, 134423 (2018).

[46] K. Hamamoto, M. Ezawa, and N. Nagaosa, Phys. Rev. B **92**, 115417 (2015).

[47] B. Göbel, I. Mertig, and O. A. Tretiakov, Phys. Rep. **895**, 1 (2021).

[48] Y. A. Kharkov, O. P. Sushkov, and M. Mostovoy, Phys. Rev. Lett. **119**, 207201 (2017).

[49] B. Göbel, A. Mook, J. Henk, I. Mertig, and O. A. Tretiakov, Phys. Rev. B **99**, 060407(R) (2019).

[50] See Supplemental Material at http://link.aps.org/supplemental/10.1103/PhysRevLett.128.227204 for the technical details of the tight-binding model and the Refs. [51,52] therein.

[51] The Schrödinger equation in a classical context: A seminar on superconductivity, The Feynman Lectures on Physics Vol. III, Chap. 21.

[52] S. Bhowal, S. Satpathy, and P. Sahu, Stud. J. Phys. **8**, 41 (2020), https://www.iopb.res.in/~sjp/82final/f1.pdf.

[53] Note that, under both time reversal and space inversion, the integrand $\mathcal{O}^n_{ij}(\vec{k}) \to -\mathcal{O}^n_{ij}(-\vec{k})$, implying that a nonzero value of the integral in Eq. (3) requires both symmetries to be broken.

[54] S. Bhowal, S. P. Collins, and N. A. Spaldin, Phys. Rev. Lett. **128**, 116402 (2022).

[55] K. T. Delaney, M. Mostovoy, and N. A. Spaldin, Phys. Rev. Lett. **102**, 157203 (2009).

[56] Y. Tokura and N. Kanazawa, Chem. Rev. **121**, 2857 (2021).

[57] L. Bo, C. Hu, L. Ji, L. Kong, R. Zhao, and X. Zhang, Phys. Status Solidi RRL **15**, 2100076 (2021).

[58] K. Shibata, X. Z. Yu, T. Hara, D. Morikawa, N. Kanazawa, K. Kimoto, S. Ishiwata, Y. Matsui, and Y. Tokura, Nat. Nanotechnol. **8**, 723 (2013).

[59] P. Milde, D. Köhler, J. Seidel, L. M. Eng, A. Bauer, A. Chacon, J. Kindervater, S. Mühlbauer, C. Pfleiderer, S. Buhrandt, C. Schütte, and A. Rosch, Science **340**, 1076 (2013).

[60] D. I. Khomskii, Nat. Commun. **3**, 904 (2012).

[61] D. I. Khomskii, Nat. Commun. **5**, 4793 (2014).

[62] Y. F. Popov, A. M. Kadomtseva, G. P. Vorob'ev, V. A. Timofeeva, D. M. Ustinin, A. K. Zvezdin, and M. M. Tegeranchi, J. Exp. Theor. Phys. **87**, 146 (1998).

[63] H. Saito, K. Uenishi, N. Miura, C. Tabata, H. Hidaka, T. Yanagisawa, and H. Amitsuka, J. Phys. Soc. Jpn. **87**, 033702 (2018).